ACS APPLIED MATERIALS & INTERFACES

Research Article

www.acsami.org

Electron-Beam-Assisted Oxygen Purification at Low Temperatures for Electron-Beam-Induced Pt Deposits: Towards Pure and High-Fidelity Nanostructures

Harald Plank,[†,‡] Joo Hyon Noh,[§,∥] Jason D. Fowlkes,[§] Kevin Lester,[§] Brett B. Lewis,[∥] and Philip D. Rack*[,§,∥]

[†]Institute for Electron Microscopy and Nanoanalsis, Graz University of Technology, Steyrergasse 17, 8010 Graz, Austria

[‡]Center for Electron Microscopy, Graz University of Technology, Steyrergasse 17, 8010 Graz, Austria

[§]Center for Nanophase Materials Sciences, Oak Ridge National Laboratory, Oak Ridge, Tennessee 37831, United States

[∥]Department of Materials Science and Engineering, University of Tennessee, Knoxville, Tennessee 37996, United States

Supporting Information

ABSTRACT: Nanoscale metal deposits written directly by electron-beam-induced deposition, or EBID, are typically contaminated because of the incomplete removal of the original organometallic precursor. This has greatly limited the applicability of EBID materials synthesis, constraining the otherwise powerful direct-write synthesis paradigm. We demonstrate a low-temperature purification method in which platinum−carbon nanostructures deposited from MeCpPtIVMe$_3$ are purified by the presence of oxygen gas during a post-electron exposure treatment. Deposit thickness, oxygen pressure, and oxygen temperature studies suggest that the dominant mechanism is the electron-stimulated reaction of oxygen molecules adsorbed at the defective deposit surface. Notably, pure platinum deposits with low resistivity and retain the original deposit fidelity were accomplished at an oxygen temperature of only 50 °C.

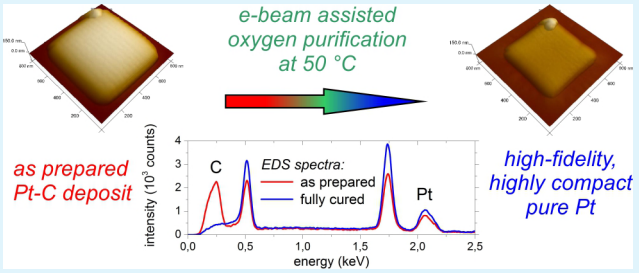

KEYWORDS: *focused electron-beam-induced deposition, platinum, nanofabrication, electron-stimulated reactions*

INTRODUCTION

Electron-beam-induced deposition (EBID) is a nanoscale synthesis method in which a scanning focused electron beam induces the local dissociation of adsorbed precursor molecules.[1] Part of the dissociated precursor typically desorbs, and the rest of the original precursor locally condenses. Because this synthesis method is a direct-write technique, EBID has been used for many applications including lithography mask repair[2−4] and nanolithography;[5,6] nanoscale welding (particularly for TEM specimen preparation);[7−10] advanced scanning probe microscopy probes;[11−13] magnetic storage, sensing, and logic applications;[14,15] nanoscale stress−strain sensors,[16−18] electron sources,[19] nano optics,[20] nanoscale gripping devices (nanotweezers),[21] and nanobio applications;[22] diodes;[23] seeds for nanofiber growth[24] and atomic layer deposition;[25] and nanoscale gas sensors.[26]

Typically, EBID is performed at room temperature, so besides the metal atoms, nonvolatile byproducts remain on the surface and incorporate in the deposited material. Because most precursors are organometallics, carbonaceous contamination is common with a usually higher atomic content than the intended metal. One important application for EBID is depositing electrodes to contact various nanoscale elements; however, because the deposits have low metal fractions, they exhibit resistivities several orders of magnitude greater than pure metals.[27−29] A few exceptions have been demonstrated, for example, Fernandez-Pacheco et al. showed near-bulk cobalt resistivity without postprocessing[30] and Klein et al. showed single-crystal tungsten nanowires from WF_6 without additional processing.[31]

Although a few precursors exhibit pure as-deposited material via EBID, most do not. Thus, much attention has been given towards both in situ and ex situ purification methods. For example, strategies include synchronized laser-assisted EBID,[32,33] annealing of the structures after deposition,[34−37] deposition onto heated substrates,[38,39] varying the deposition parameters (beam current, precursor flux, and scanning method),[36,40,41] introducing reactive gases into the chamber during deposition,[42] the use of carbon-free precursors,[40,43−45] and various other in situ and ex situ processes.[17,18,36,46] For more information on purification methods, see Botman et al.[47]

In this study, we investigate the postgrowth purification of platinum−carbon deposits via electron-beam-induced exposure in a low-temperature oxygen ambient. The original Pt−C$_x$

Received: October 15, 2013
Accepted: December 30, 2013
Published: December 30, 2013

(where x typically varies from 4−8 depending on the deposition conditions) deposits were grown via EBID using the trimethyl(methylcyclopentadienyl)platinum(IV) (MeCpPt^{IV}Me$_3$) precursor. Of relevance to our work, Wnuk et al.[48] has shown that under low current fluxes the initial electron-stimulated reaction occurs via the dissociation of a methyl group bonded to the Pt atom. Thus, at low doses, the Pt/C ratio of the deposit is nominally 1:8, whereas the parent molecule is 1:9; the resultant deposit is a mixture of amorphous carbon and metallic platinum clusters. Plank et al.,[49] Schwalb et al.,[18] and Poratti et al.[17] have shown the effect that postdeposition electron exposure has on the Pt−C$_x$ EBID deposit functionality. Namely, both showed a decrease in resistivity from ∼1 × 10^7 to ∼1 × 10^4 $\mu\Omega$ cm and described two regimes for the change in resistivity with electron exposure: (1) electron-stimulated reduction of carbon byproducts in the deposit and metallic Pt cluster ripening and (2) a graphitization stage of the amorphous carbon at longer electron exposures. Other postexposure thermal treatments are also specifically relevant to this work: Botman et al. showed ∼70 atom % pure platinum deposits from EBID followed by a 10 min anneal at 500 °C in an O$_2$ environment.[35] Finally, more recently, Mehendale et al. reported the platinum purity deposited as a function of temperature with a subsequent oxygen anneal with and without concurrent electron exposure. They showed that ∼60 nm thick Pt−C$_x$ EBID deposits could be purified with a 120 °C substrate heat in an O$_2$ environment via 5 keV to 24 nA electron exposure with a curing rate of about 6 min μm^{-2} at an electron dose of about 8.6 × 10^3 nC μm.[2,37]

In this article, we extend the purification of PtC$_x$ (where our as-deposited composition was $x \sim 4$) EBID deposits (5 keV, 98 pA, 500 × 500 nm) via electron-stimulated carbon removal to low oxygen temperatures, which enables the purification of temperature-sensitive samples that cannot withstand elevated temperatures. In situ energy-dispersive X-ray spectroscopy (EDS) was used to monitor the progressive carbon removal, and we demonstrate that judicious electron and O$_2$ parameters can efficiently remove the carbon byproduct at low temperature. Lower temperatures are advantageous because they minimize thermal drift in the electron microscope and can reduce interdiffusion of other materials for device applications with low-thermal-budget tolerances. Furthermore, the typically severe porosity/morphological changes that occur at higher temperature processing[37,50] can be entirely avoided.

Initially, the effective purification time as a function of the original deposit height was performed under conditions in which the Ar−O$_2$ (80:20) gas was heated to 78 °C at a gas flow to achieve background oxygen pressure of 7 × 10^{-6} mbar (base pressure 9 × 10^{-7} mbar). Estimations on the basis of the GIS proximity (see Methodology and Supporting Information 1 information) suggest a localized pressure on the order of 1.3 × 10^{-3} mbar (2.6 × 10^{-4} mbar O$_2$) at the curing area. Figure 1a compares the uncorrrected EDS spectra of as-deposited (red) and purified (blue) 60 nm Pt−C EBID deposits.

Also included in the plot is a spectrum for the SiO$_2$/Si substrate (grey) and a platinum reference film (green). Figure 1b illustrates background-corrected in situ EDS spectra of the carbon peak collected for an ∼60 nm thick EBID deposit as a function of electron−O$_2$ exposure time performed at 5 keV/1.6 nA (see Supporting Information 2). Figure 2a shows the integrated carbon peak area as a function of time, which shows that the minimum time for purifying the 60 nm thick film is ∼5 min (see Methodology and Supporting Information 3 for more details). Figure 2b is a plot of the minimum time per square micrometer footprint to purify the Pt deposit as a function of original EBID deposit thickness. Interestingly, the purification efficiency (thickness divided by purification time for constant conditions) actually increases with increasing thickness, as the second derivative of the plot of Figure 2b is negative.

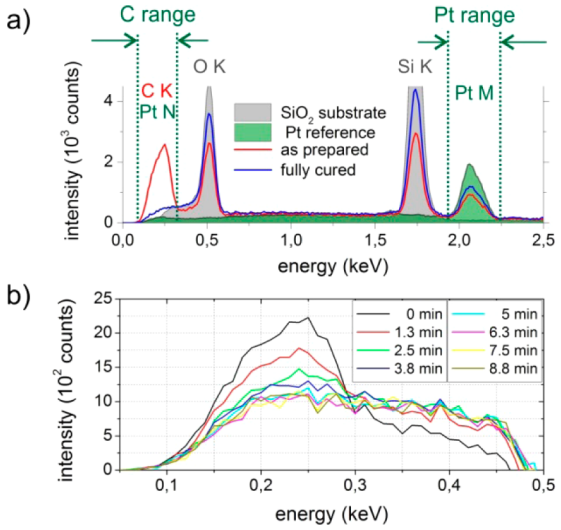

Figure 1. (a) EDS reference measurements for Pt (green) and SiO$_2$ (grey) obtained by ideal EDS settings (see Methodology). The calculated ratio of Pt−N/Pt−M is about 0.09 and was obtained via integrating the Pt−N peak range (120−330 eV) and Pt−M range (1950−2220 eV) as indicated; the graphs also show the uncorrected spectra for an originally 60 nm thick Pt−C deposit after deposition (red) and after full curing (blue) using a 78 °C gas temperature and a chamber pressure of 7 × 10^{-6} mbar, revealing that the carbon area is nearly identical to the convolution of the SiO$_2$ and Pt reference spectra shown in grey and green, respectively. (b) Time evolution of the in situ carbon range, revealing the decreasing and saturating behavior at a 78 °C gas temperature and 7 × 10^{-6} mbar chamber pressure (in situ details can be found in the Supporting Information).

We assume that two effects contribute to the increased purification efficiency with increasing thickness: (1) the energy-deposited subsurface creates dangling bonds in the Pt−C matrix, which makes it easier to purify or remove the carbon when the surface is exposed to the oxygen/electron beam and (2) the electron beam is slowed in route to the underlying material and has a higher effective cross-section for stimulating the reaction. Although the curing efficiency appears to increase with increasing thickness, the purification depth appears to saturate at ∼40−60 nm at this pressure, which is consistent with the 5 keV high-temperature process reported by Mehendale et al.[37] and the effective electron-curing depth by Plank et al.[49] Although absolute quantification is difficult because the Pt N peak overlaps the carbon K region (Figure 1a), Figure 2c is a plot of the integrated C/Pt ratio of the final EDS spectra after 45 min of O$_2$−electron beam exposure, which illustrates that below ∼60 nm the Pt/C ratio approaches the Pt N/M ratio of about 0.09 that was experimentally found for the pure Pt sample illustrated in Figure 1a (see Methodology and Supporting Information 3 for full data sets for each thickness). As described by Mehendale et al., the increasing carbon content in the thicker films is likely due to either a combination of insufficient oxygen permeation to the underlying film and/or redeposition of the CO$_x$ byproduct in the presumably tortuous path. Figure 3a shows the cumulative energy loss for ∼39 062

dx.doi.org/10.1021/am4045458 | ACS Appl. Mater. Interfaces 2014, 6, 1018−1024

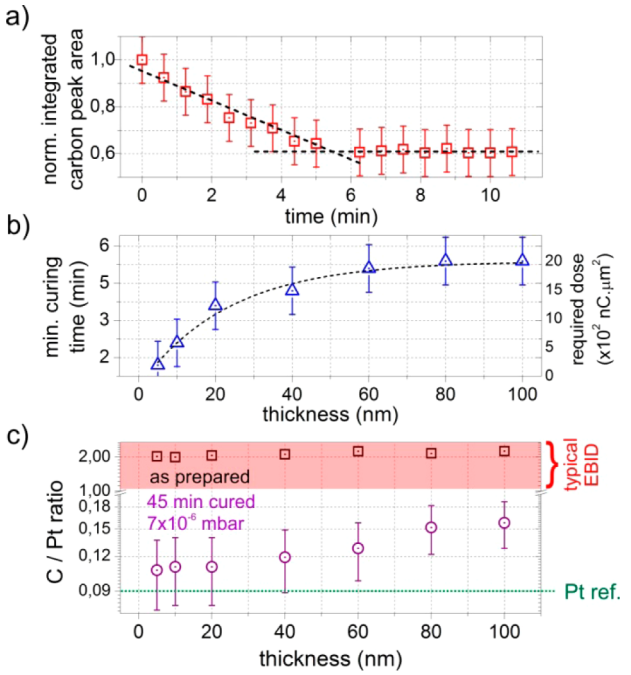

Figure 2. (a) Time evolution of the integrated and normalized in situ measured carbon intensities shown in Figure 1b using a 78 °C O_2 temperature and 7×10^{-6} mbar chamber pressure of an originally 60 nm Pt−C deposit. (b) Required purification time per square micrometer as a function of the original deposit thickness; the electron dose is given on the right axis. (c) C/Pt ratios for as-prepared (squares) and purified deposits (purple circles) as a function of the original deposit thickness. The Pt reference value was found to be 0.09 (dotted green line) based on the Pt reference spectra in Figure 1a (green curve).

(5 keV) electrons, illustrating that most of the energy is deposited in the top ∼100 nm of the deposit. Figure 3b is the energy loss for 5 keV electrons in pure platinum, which is limited to the top ∼20 nm because of the high density of platinum.

To rationalize the initial results, Table 1 illustrates the approximate localized O_2 flux (assuming a localized pressure of 2.6×10^{-4} mbar), electron flux (1.6 nA and ∼20 nm FWHM electron beam), and the approximate areal carbon density of

Table 1. Estimated Electron and Oxygen Parameters[a]

localized O_2 flux	1×10^3 O_2 nm^{-2} s^{-1}
localized electron flux	3×10^7 e^- nm^{-2} s^{-1}
areal carbon density	13 carbon nm^{-2}
total areal dose (for 5 min for 500 × 500 nm box)	1.3×10^7 e^- nm^{-2}
effective electron irradiation time	0.4 s nm^{-2}
estimated carbon atoms in 1 nm^2 × 60 nm (PtC_4)	3100 carbon atoms
estimated total O_2 molecules impinging on 1 nm^2 area in 5 min cure	415 O_2 nm^{-2}

[a]See Supporting Information 4 for calculation details.

the PtC_4. Additionally, on the basis of the ∼5 min time for the 60 nm thick sample to purify, the total areal dose, effective electron irradiation time per square nanometer for the rastered beam, and the total number of carbon atoms in a 1 × 1 nm^2 area × 60 nm thick purified sample is estimated. Interestingly, the ratio of the localized electron flux to the oxygen flux is ∼3×10^4, and the ratio of the oxygen atoms that impinge on the surface during cumulative electron-beam exposure to the total number of carbon atoms etched is ∼0.1 (see Supporting Information 4 for calculation details). Thus, the purification regime that emerges is one in which the electron flux is approximately 4 orders of magnitude greater than the oxygen flux and thus the carbon etching is assumed to be oxygen mass-transport limited (MTL).

For additional context regarding our initial observations, Hopf et al.[51] studied amorphous carbon etching via energetic argon ion irradiation in a molecular oxygen ambient as a function of ion current and energy, oxygen pressure, and substrate temperature. Their study revealed several etch processes, namely, (1) physical sputtering, (2) chemical sputtering by direct reaction of incoming O_2 at unperturbed or unactivated carbon sites, (3) chemical sputtering by the ion-induced reaction of oxygen molecules adsorbed onto carbon sites activated by ion bombardment which have higher O_2 binding energy, (4) thermal chemical erosion, and (5) an ion-induced enhancement of thermal chemical erosion. Although, of course, the sputtering mechanisms are not relevant in our study because the electron mass and velocity are not appropriate for sputtering, electron-stimulated reactions and desorption processes are envisioned to occur analogous to steps 2 and 3, namely, (2) electron-stimulated reactions of O_2

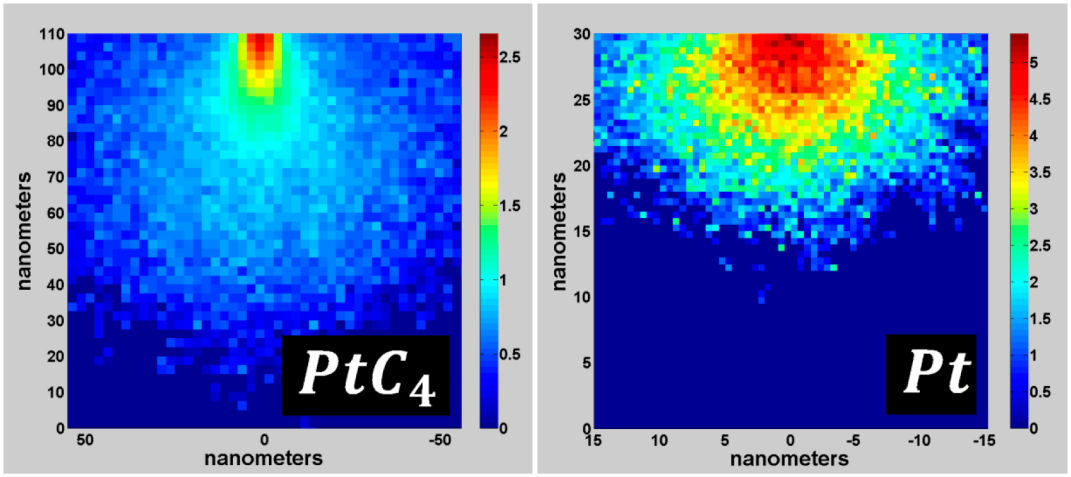

Figure 3. Simulated energy-loss profiles for 39 062 (5 keV) electrons in (a) PtC_4 and (b) pure Pt. Note the simulated electron-penetration depth is consistent with the thickest as-deposited PtC_4 (110 nm) and resultant Pt (30 nm) purified thickness.

adsorbed on unactivated sites that have albeit very low residence times and (3) an electron-stimulated reaction of O_2 that are adsorbed onto so-called activated carbon sites with higher O_2 binding energy. Higher temperatures, similar to what Medendale et al. studied and observed, could also initiate thermal and electron-stimulated thermal erosion similar to steps 4 and 5. It is also worth mentioning that typical binding energies for molecular oxygen on graphite and nanotubes are on the order of 18−25 meV (or adsorption energy of −18 to −25 meV);[52,53] thus, the equilibrium coverage of O_2 on unperturbed carbon is extremely low.

As will be described later, electron dissociation of simultaneously adsorbing oxygen (analogous to step 2) and dissociation of oxygen adsorbed onto high-binding-energy sites created by electron interactions (analogous to step 3) are suspected to govern the observed purification. The specific contributions of these two mechanisms under various conditions will be elucidated below. On the basis of the apparent O_2 mass-transport-limited regime, the first obvious parameter to vary was the oxygen gas-flow rate. Figure 4a illustrates the effective purification time (see Supporting Information 5 for details) of ∼110 nm thick PtC_4 EBID deposits as a function of measured chamber pressure (and localized pressure estimated to range from $\sim 2.6 \times 10^{-4}$ to 3×10^{-3} mbar). As is clear from the Figure 4a, the purification time decreases with increasing oxygen pressure and saturates for chamber pressures above 3×10^{-5} mbar, equivalent with a local O_2 pressure of about 1.3×10^{-3} mbar. Referring to Hopf et al.'s work,[51] we attribute the increased purification rate to the increased equilibrium coverage of the molecular oxygen at the point in which the rastered beam arrives at the exposed PtC_4 area, thereby increasing the simultaneous electron dissociation and reaction of adsorbed oxygen during the electron on-time. AFM and postexposure EDS analysis revealed that the saturated pad volume varied as a function of pressure. Figure 4b shows AFM height images (same *xyz* scales) of an as-prepared (left) and fully cured (right) deposit performed at the highest pressure, which indicates a large volume loss. Figure 4c summarizes the pressure-dependent volume loss determined via AFM analysis (circles) and the calculated values based on the residual carbon estimated via EDS (squares). The purification process is envisioned to occur from the top down and thus transport of O_2 molecules to the underlying carbon matrix is necessary. Thus, the oxygen transport is not simply a simple first-order physisorption process; it requires diffusion of the oxygen molecules to the reaction region and byproducts away from the reaction region.

At higher pressures, it appears that the transport is able to supply adequate oxygen to purify the full ∼110 nm thick EBID deposit, whereas at lower pressure, only partial purification was achieved. Also demonstrated in Figure 3 is the energy-loss simulation of a 5 keV beam in pure platinum, which illustrates that the beam interaction depth is comparable to the ∼30 nm to the residual platinum thickness measured after the ∼110 nm PtC_4 is purified. Future studies will investigate the electron-beam energy dependence on the process because a higher beam energy should be able to purify thicker deposits, albeit likely at a lower rate because of (1) lower secondary electron yields at higher energy, (2) lower electron-stimulated cross sections at higher energy, and (3) reduced oxygen transport for thicker films. In summary, the increased oxygen pressure increases the flux of oxygen and thus (1) increases the simultaneous electron/O_2 reaction contribution and (2) the equilibrium

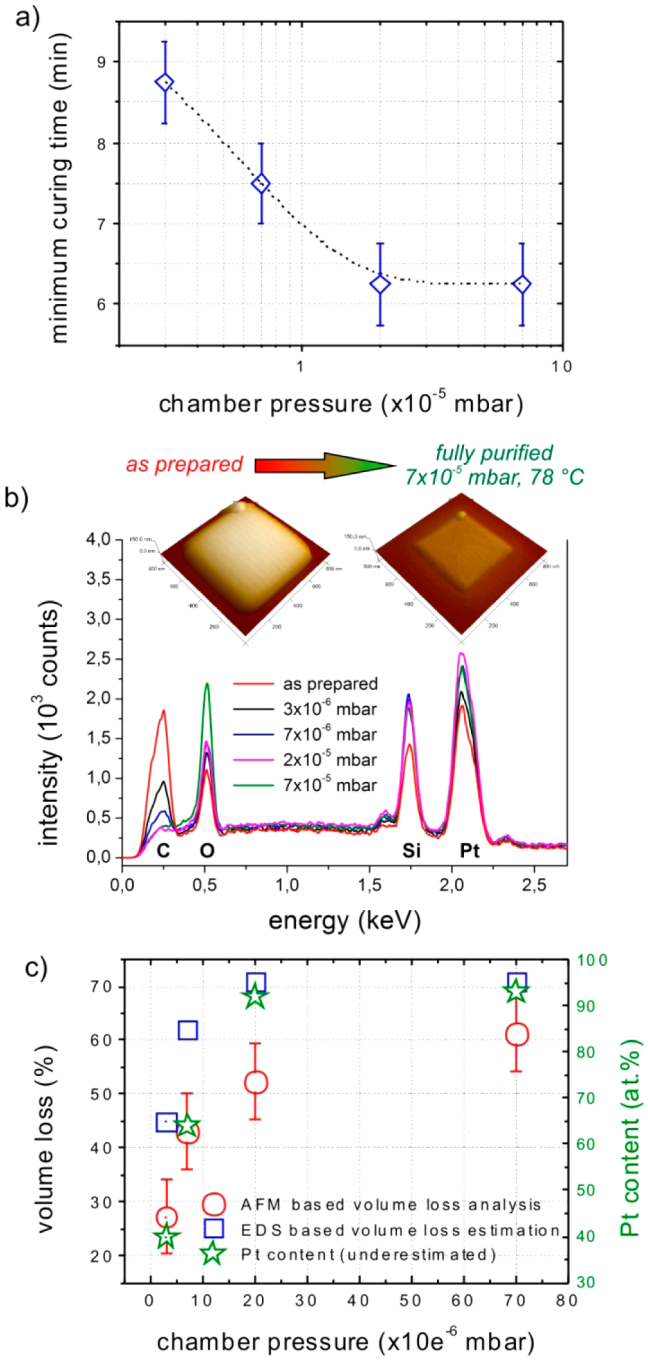

Figure 4. Oxygen-assisted electron-beam purification of an initially 110 nm thick Pt−C deposit at a constant gas temperature of 78 °C. (a) Minimum curing times versus O_2 chamber pressure. (b) AFM height images of an as-prepared (left) and a fully purified deposit (performed at highest O_2 pressure) together with uncorrected EDS spectra before (red) and after purification for different pressures (see legend). (c) Summary of AFM- and EDS-based volume loss (circles and squares, respetively) together with Pt content (stars) based on uncorrected EDS spectra (values are underestimated because of Si_L contribution at C areas; see panel b, Methodology, and Supporting Information).

coverage of oxygen adsorbed on activated carbon sites (particularly deeper into the evolving purified deposit). Thus, it is difficult to discriminate specifically which mechanism is dominating in this pressure range. In either case, at the highest pressure, the observed saturation suggests we have apparently

dx.doi.org/10.1021/am4045458 | ACS Appl. Mater. Interfaces 2014, 6, 1018−1024

shifted the carbon removal to an electron-limited regime. These details will be explored in the future.

To study the electron/O_2 purification further, the O_2 gas temperature was gradually reduced from 78 °C to room temperature at a constant chamber pressure of 5.5×10^{-5} mbar. Figure 5a illustrates the requisite purification times for a 110 nm thick PtC_4 EBID deposit, revealing a linear decrease for decreasing temperatures from 78 to 50 °C. This trend can be understood as effectively increasing the O_2 residence time and thus increasing the oxygen coverage by lowering the temperature, which is similar to what Hopf et al.[51] observed in the range from −173 to +127 °C. Mass-loss calculations from AFM and EDS measurements confirm that each of these materials were fully purified (see the temperature series in Supporting Information 6). Nonintuitively, when the temperature is reduced below 50 °C, the purification is arrested and the carbon peak actually increases. Complementary studies (see Supporting Information 7 for detailed in situ EDS spectra illustrating competitive residual Pt deposition) revealed that competitive redeposition from residual $MeCpPt^{IV}Me_3$ precursor in the GIS is occurring that has a reported adsorption energy of ~0.55 eV.[48] Thus, in the temperature range studied, the residence time (assuming an attempt frequency of 1×10^{13} s^{-1}) is ~195, 37, and 8 μs at 25, 50, and 78 °C, respectively. Over the narrow temperature range of 78 to 50 °C, we attribute the increased purification rate to an increase in the effective O_2 equilibrium coverage and thus analogous to Hopf et al.'s process 3 and their observed increased carbon etch rate at lower temperature. As can be seen in Figure 5b from an SEM image of resultant purified morphology, the treated deposits do not show the typical large porosity often found for annealed and electron-beam O_2-cured samples at high temperatures.[37,41] The specific nanostructure of the resultant deposit will be confirmed via transmission electron microscopy in a subsequent work. The surface roughness found via AFM is only slightly higher than for as-fabricated deposits (1.5 vs 0.9 nm), and even the footprint size is maintained, which is essential to exploit the advantages of EBID for complex nanostructuring. On the basis of our initial studies, we expect that the purification process could be extended and improved at room temperature. We will be investigating system modifications to the GIS to mitigate the residual $MeCpPt^{IV}Me_3$ that is competing with the purification at lower temperatures.

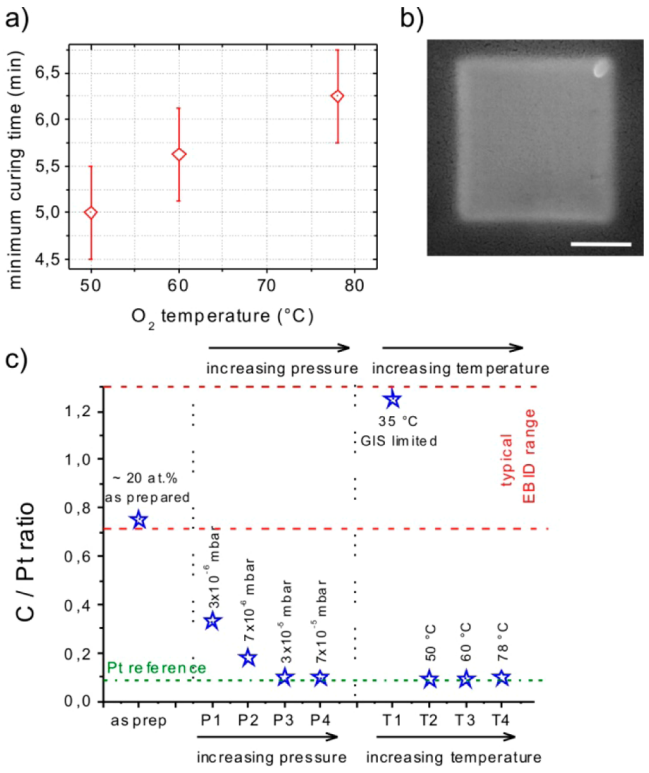

Figure 5. (a) Temperature dependence of the minimum purification times for a constant O_2 pressure of 5.5×10^{-5} mbar. (b) SEM image of an initially 110 nm deposit, fully purified under optimal conditions of 50 °C O_2 gas temperature at a pressure of 5.5×10^{-5} mbar, revealing a and distortion-free morphology (scale bar is 200 nm). (c) Summary plot of C/Pt ratios as a measure for purity with an experimentally determined threshold of about 0.09 (green bottom line).

Figure 5c summarizes the C/Pt ratios for the pressure and temperature variation. As can be seen, for ideal settings, the ratios closely approach 0.09, which was found as the reference value for pure Pt (lower dotted line, see also Figure 1a and Methodology). The lowest values are achieved for sufficiently high local pressures (>3×10^{-5} mbar) and low temperatures (50 °C). In particular, it is found that the morphology becomes even more compact for the lowest curing temperatures of 50 °C using comparable mass-loss analysis shown above.

To estimate conductivity of the electron-O_2-purified platinum material, two-point probe tests of an electron-O_2-treated sample that was ~100 nm thick (three sequentially treated ~110 nm EBID layers) and 500 nm wide and long was measured. The measured resistance was 37 Ω relative to a comparable untreated EBID sample that was 4.5×10^7 Ω. The upper estimate of the treated sample resistivity (as the contact resistance is present in the two-point measurement) is therefore ~370 $\mu\Omega$ cm, which is more than six orders of magnitude lower than the as-deposited PtC_4 (4.5×10^8 $\mu\Omega$ cm). Future studies will include contact resistance and four-point probe measurements to determine more accurately the electron-O_2 platinum resistivity, as we anticipate that it is close to bulk values.

CONCLUSIONS

Nanoscale electron-beam induced PtC_4 deposits were purified by irradiating the nanoscale patterns with 5 keV electrons in an oxygen ambient. Two specific mechanisms are believed to contribute to the carbon removal, namely, (1) an electron-stimulated reaction from simultaneous oxygen-electron adsorption impingement and (2) electron-stimulated reaction of oxygen previously adsorbed onto high-binding-energy sites created by the electron exposure. Studies revealed that increasing oxygen pressure increases the purification rate as does decreasing the oxygen gas temperature. Both of these observations suggest that these process regimes are limited by the oxygen mass transport except at the highest oxygen partial pressure studied in which the rate saturated. EDS measurements reveal that within the experimental accuracy all of the residual carbon in ~110 nm thick EBID deposits can be removed (which is the approximate electron penetration depth of the 5 keV electrons in PtC_4). Two-point probe electrical measurements reveal that the upper limit of the resultant platinum resistivity is 370 $\mu\Omega$ cm, which includes the contact resistance of the system.

METHODOLOGY

Deposition and electron-O_2 purification experiments were performed with a FEI NOVA 600 dual-beam system equipped with a OMNI GIS

I system (Oxford Instruments) and a plasma cleaner (XEI Scientific, Inc., Evactron Decontaminator). The gas-injection system (GIS) was installed in an angle of 52° with respect to the sample surface. The inner and outer diameter of the nozzle end is 750 and 500 μm, respectively, and the lower end of the nozzle was placed at a distance of 120 μm to the sample surface. The experiments have been performed in a distance of 100 μm wrt the GIS. Samples of 10 × 10 mm^2 Si with 100 nm SiO_2 were cleaned by two methods that were effective at removing the adventitious carbon: (1) a 900 °C Ar−H_2 anneal for 10 min or (2) washing in isopropanol for 5 min followed by CO_2 cleaning and 5 min microwave plasma cleaning. After immediate transfer to the dual-beam microscope, the samples and chamber were further cleaned by the attached plasma cleaner at a background pressure of 4 × 10^{-3} mbar using ambient air for 1 h. Electrical measurements were performed on prestructured two-point geometries with 500 nm line and space using Cr−Au electrodes. After establishing a chamber background pressure between ∼0.9 and 1.1 × 10^{-6} mbar, the deposits were fabricated using MeCpPt(IV)Me_3 precursor. The special design of the OMNI GIS I uses a Pt precursor temperature of 33 °C together with an N_2 co-flow heated at 50 °C (both temperatures were equilibratedfor at least 1 h before deposition). After establishing a stable precursor/carrier gas flow, the chamber pressure increased to 1.5 × 10^{-5} mbar, and an additional wait time of 5 min was introduced before patterning to establish equilibrium coverage on the SiO_2 surface. Pt−C deposits were fabricated using a 5 keV/98 pA beam energy and current, respectively, via the FEI internal patterning generator under focused conditions. The pattern footprint was 500 × 500 nm^2 for basic samples and 2000 × 500 nm^2 for electrical four-point measurements. A serpentine scanning strategy was used with a point pitch of 13.5 nm and 10 μs pixel dwell time. To achieve different thicknesses, the number of loops was varied and correlated with atomic force microscopy measurements. After deposition, the OMNI GIS I was purged with N_2 as purging gas at 50 °C for 20 min to clean the GIS. For the electron-beam purification, Ar/O_2 (80:20) was used and heated at different temperatures ranging from 35 to 78 °C (intrinsic upper limit). The OMNI GIS I system uses two valves to control the gas flow and allows in situ monitoring of the nozzle pressure, which was used to establish stable gas-flow conditions during curing (temperatures and final chamber pressures are specified in the main text). Oxygen-assisted e-beam curing was performed at 5 keV/1.6 nA via live imaging under focused conditions. The horizontal image width was 934 nm with 1024 pixel horizontal resolution equal to a point pitch of ∼0.91 nm. Dwell times of 1 μs were used during oxygen-assisted e-beam curing, whereas the beam shift together with the alignment rectangle were used to ensure that the 500 × 500 nm^2 Pt−C deposit is always centered. Energy-dispersive X-ray spectroscopy (EDS) was performed with an EDAX Genesis X-ray microanalysis system spectrometer. In situ characterization was done as follows: after establishing a constant curing pressure, a reference spectrum was taken for 30 s at clean SiO_2 areas with the same magnification, pixel resolution, and dwell times as those used for the oxygen-assisted e-beam curing specified above. To estimate the contamination influence of the substrate, a subsequent spectra was taken from the same area after about 2 min of permanent exposure and then compared to the first spectra, which was always found to be practically identical. In situ curing EDS spectra were acquired in time steps between 1 and 5 min, depending on the experiment. For analysis, the in situ spectra were corrected by the reference spectra taken on SiO_2 (see Supporting Information 2). To track the temporal carbon evolution, corrected peak areas between 120 and 330 eV were integrated and used as an indicator for carbon removal (see Supporting Information 3, 5, and 6). Please note that the obtained values do not allow for detailed quantitative analysis but give only the qualitative behavior of the temporal evolution. After curing was finished, the deposits were remeasured under ideal EDS conditions using EDS mode 3 of the NOVA 600. Because the thin deposits investigated still show Si and O peaks, a reliable quantitative analysis was not possible but leads to (1) overestimated Pt values for background corrected spectra or (2) underestimated Pt values because of the Si_L peak in the C area (see Supporting Information 7). Nevertheless, the latter approach was used for calculating the data shown in Figure 4c. Alternatively, as suggested by Mehendale et al.,[37] we used the uncorrected C/Pt ratio using integration ranges of 120−300 and 1950−2220 eV for C and Pt, respectively, which represent again slightly underestimated values because of the Si_L peak (relevant data are shown in Figure 5c). As a reference value, we characterized a Pt sample under the same imaging conditions to access the expected C/Pt ratio for pure Pt, which was found to ∼0.09. The Pt reference sample was subsequently investigated several times at the same spot to prove a very low C contamination, which would convolute this reference value towards higher values. Hence, the finally obtained C/Pt ratios of the cured deposits (see Supporting Information 8) can be used to estimate their purities by approaching the C/Pt reference value of 0.09. Atomic force microscopy (AFM) measurements were performed with a Dimension 3100 microscope (Digital Instruments, Bruker) operated with a Nanoscope III controller and a phase extender box using Olympus OMCL TS-160 cantilever in tapping mode. Electrical properties were measured by a two-point method using interdigitized (IDT) electrode structure. Voltage was swept and current was measured using a Keithley model 2400. For the as-deposited and cured Pt, voltages were swept from 1 to 10 mV with a 1 mV step and from 200 to 1100 μV with a 100 μV step, respectively.

■ ASSOCIATED CONTENT

Supporting Information

Localized pressure determination, in situ EDS, thickness dependency at constant pressure (7 × 10^{-6} mbar) and O_2 temperature (78 °C), calculations for estimated oxygen and electron parameters, pressure dependence of 110 nm thick deposits at constant O_2 temperatures (78 °C), temperature dependence of 110 nm thick deposits at 5.5 × 10^{-5} mbar, residual Pt precursor contamination as a function of gas temperature, and idealized EDS. This material is available free of charge via the Internet at http://pubs.acs.org.

■ AUTHOR INFORMATION

Corresponding Author

*E-mail: prack@utk.edu; Tel: +1 865-974-5344.

Notes

The authors declare no competing financial interest.

■ ACKNOWLEDGMENTS

This research was conducted at the Center for Nanophase Materials Sciences, which is sponsored at Oak Ridge National Laboratory by the Scientific User Facilities Division, Office of Basic Energy Sciences, U.S. Department of Energy. HP acknowledges the support from Prof. Ferdinand Hofer and the Austrian Cooperative Research (ACR) and the Graz University of Technology in Austria. BBL acknowledges support via the University of Tennessee Chancellor's Fellowship program. JN and HP acknowledge support from Semiconductor Research Corporation (SRC-2012-In-2310). The authors acknowledge Cheryl Hartfield at Omniprobe, Inc. (an Oxford Instruments Company) for assistance with the OmniGIS gas injection system.

■ REFERENCES

(1) *Nanofabrication Using Focused Ion and Electron Beams: Principles and Applications*; Utke, I., Moshkalev, S., Russell, P., Eds.; Oxford University Press: New York, 2012.

(2) Lassiter, M. G.; Liang, T.; Rack, P. D. *J. Vac. Sci. Technol., B* **2008**, *26*, 963−967.

(3) Liang, T.; Frendberg, E.; Lieberman, B.; Stivers, A. *J. Vac. Sci. Technol., B* **2005**, *23*, 3101−3105.

(4) Edinger, K.; Becht, H.; Bihr, J.; Boegli, V.; Budach, M.; Hofmann, T.; Koops, H. W. P.; Kuschnerus, P.; Oster, J.; Spies, P.; Weyrauch, B. *J. Vac. Sci. Technol., B* **2004**, *22*, 2902−2906.
(5) Guan, Y.; Fowlkes, J. D.; Retterer, S. T.; Simpson, M. L.; Rack, P. D. *Nanotechnology* **2008**, *19*, 505302.
(6) Heerkens, C. T. H.; Kamerbeek, M. J.; van Dorp, W. F.; Hagen, C. W.; Hoekstra, J. *Microelectron. Eng.* **2009**, *86*, 961−964.
(7) Banhart, F. *Nano Lett.* **2001**, *1*, 329−332.
(8) Madsen, D. N.; Molhave, K.; Mateiu, R.; Rasmussen, A. M.; Brorson, M.; Jacobsen, C. J. H.; Boggild, P. *Nano Lett.* **2003**, *3*, 47−49.
(9) Ding, W.; Dikin, D. A.; Chen, X.; Piner, R. D.; Ruoff, R. S.; Zussman, E.; Wang, X.; Li, X. *J. Appl. Phys.* **2005**, *98*, 4905−4911.
(10) Brintlinger, T.; Fuhrer, M. S.; Melngailis, J.; Utke, I.; Bret, T.; Perentes, A.; Hoffmann, P.; Abourida, M.; Doppelt, P. *J. Vac. Sci. Technol., B* **2005**, *23*, 3174−3177.
(11) Noh, J. H.; Nikiforov, M.; Kalinin, S. V.; Vertegel, A. A.; Rack, P. D. *Nanotechnology* **2010**, *21*, 365302.
(12) Roberts, N. A.; Noh, J. H.; Lassiter, M. G.; Guo, S.; Kalinin, S. V.; Rack, P. D. *Nanotechnology* **2012**, *23*, 145301.
(13) Utke, I.; Hoffmann, P.; Berger, R.; Scandella, L. *Appl. Phys. Lett.* **2002**, *80*, 4792−4794.
(14) Fernandez-Pacheco, A.; De Teresa, J. M.; Cordoba, R.; Ibarra, M. R.; Petit, D.; Read, D. E.; O'Brien, L.; Lewis, E. R.; Zeng, H. T.; Cowburn, R. P. *Appl. Phys. Lett.* **2009**, *94*, 192509-1−192509-3.
(15) Serrano-Ramon, L.; Cordoba, R.; Rodriguez, L. A.; Magen, C.; Snoeck, E.; Gatel, C.; Serrano, I.; Ibarra, M. R.; De Teresa, J. M. *ACS Nano* **2011**, *5*, 7781−7787.
(16) Huth, M.; Porrati, F.; Schwalb, C.; Winhold, M.; Sachser, R.; Dukic, M.; Adams, J.; Fantner, G. *Beilstein J. Nanotechnol.* **2012**, *3*, 597−619.
(17) Porrati, F.; Sachser, R.; Schwalb, C. H.; Frangakis, A. S.; Huth, M. *J. Appl. Phys.* **2011**, *109*, 063715-1−063715-7.
(18) Schwalb, C. H.; Grimm, C.; Baranowski, M.; Sachser, R.; Porrati, F.; Reith, H.; Das, P.; Muller, J.; Volklein, F.; Kaya, A.; Huth, M. *Sensors* **2010**, *10*, 9847−9856.
(19) Weber, M.; Rudolph, M.; Kretz, J.; Koops, H. W. P. *J. Vac. Sci. Technol., B* **1995**, *13*, 461−464.
(20) Perentes, A.; Bachmann, A.; Leutenegger, M.; Utke, I.; Sandu, C.; Hoffmann, P. *Microelectron. Eng.* **2004**, *73-74*, 412−416.
(21) Boggild, P.; Hansen, T. M.; Tanasa, C.; Grey, F. *Nanotechnology* **2001**, *12*, 331−335.
(22) Fowlkes, J. D.; Doktycz, M. J.; Rack, P. D. *Nanotechnology* **2010**, *21*, 5303−5311.
(23) Miura, N.; Ishii, H.; Shirakashi, J.-I.; Yamada, A.; Konagai, M. *Appl. Surf. Sci.* **1997**, *113-114*, 269−273.
(24) Mukawa, T.; Okada, S.; Kobayashi, R.; Fujita, J.; Ishida, M.; Ichihashi, T.; Ochiai, Y.; Kaito, T.; Matsui, S. *Jpn. J. Appl. Phys.* **2005**, *44*, 5639−5640.
(25) Mackus, A. J. M.; Mulders, J. J. L.; van de Sanden, M. C. M.; Kessels, W. M. M. *J. Appl. Phys.* **2010**, *107*, 116102-1−116102-3.
(26) Kolb, F.; Schmoltner, K.; Huth, M.; Hohenau, A.; Krenn, J.; Klug, A.; List, E. J. W; Plank, H. *Nanotechnology* **2013**, *24*, 305501.
(27) Randolph, S. J.; Fowlkes, J. D.; Rack, P. D. *Crit. Rev. Solid State Sci.* **2006**, *31*, 55−89.
(28) Utke, I.; Hoffmann, P.; Melngailis, J. *J. Vac. Sci. Technol., B* **2008**, *26*, 1197−1276.
(29) Dorp, W. F. v.; Hagen, C. W. *J. Appl. Phys.* **2008**, *104*, 1301−1342.
(30) Fernandez-Pacheco, A.; De Teresa, J. M.; Cordoba, R.; Ibarra, M. R. *J. Phys. D: Appl. Phys.* **2009**, *42*, 055005.
(31) Klein, K. L.; Randolph, S. J.; Fowlkes, J. D.; Allard, L. F.; Meyer, H. M., III; Simpson, M. L.; Rack, P. D. *Nanotechnology* **2008**, *19*, 345705.
(32) Roberts, N. A.; Fowlkes, J. D.; Magel, G. A; Rack, P. D. *Nanoscale* **2013**, *5*, 408−415.
(33) Roberts, N. A.; Magel, G. A.; Hartfield, C. D.; Moore, T. M.; Fowlkes, J. D.; Rack, P. D. *J. Vac. Sci. Technol., A* **2012**, *30*, 041404−041406.
(34) Gopal, V.; Radilovic, V. R.; Daraio, C.; Jin, S.; Yang, P.; Stach, E. A. *Nano Lett.* **2004**, *4*, 2059−2063.
(35) Botman, A.; Mulders, J. J. L.; Weemaes, R.; Mentink, S. *Nanotechnology* **2006**, *17*, 3779−3785.
(36) Langford, R. M.; Wang, T. X.; Ozkaya, D. *Microelectron. Eng.* **2007**, *84*, 784−788.
(37) Mehendale, S.; Mulders, J. J. L.; Trompenaars, P. H. F. *Nanotechnology* **2013**, *24*, 145303.
(38) Cordoba, R.; Sese, J.; De Teresa, J. M.; Ibarra, M. R. *Microelectron. Eng.* **2010**, *87*, 1550−1553.
(39) Mulders, J. J. L.; Belova, L. M; Riazanova, A. *Nanotechnology* **2011**, *22*, 055302.
(40) Botman, A.; Hesselberth, M.; Mulders, J. J. L. *Microelectron. Eng.* **2008**, *85*, 1139−1142.
(41) Plank, H.; Gspan, C.; Dienstleder, M.; Kothleitner, G.; F, H. *Nanotechnology* **2008**, *19*, 485302.
(42) Langford, R. M.; Ozkaya, D.; Sheridan, J.; Chater, R. *Microsc. Microanal.* **2004**, *10*, 1122−1123.
(43) Wang, S.; Sun, Y.-M.; Wang, Q.; White, J. M. *J. Vac. Sci. Technol., B* **2004**, *22*, 1803−1806.
(44) Ervin, M. H.; Chang, D.; Nichols, B.; Wickenden, A.; Barry, J.; Melngailis, J. *J. Vac. Sci. Technol., B* **2007**, *25*, 2250−2254.
(45) Takeguchi, M.; Shimojo, M.; Furuya, K. *Appl. Phys. A* **2008**, *93*, 439−442.
(46) Frabboni, S.; Gazzadi, G. C.; Felisari, L.; Spessot, A. *Appl. Phys. Lett.* **2006**, *88*, 213116-1−213116-3.
(47) Botman, A.; Mulders, J. J. L; Hagen, C. W. *Nanotechnology* **2009**, *20*, 372001.
(48) Wnuk, J. D.; Gorham, J. M.; Rosenberg, S. G.; Dorp, W. F. v.; Madey, T. E.; Hagen, C. W.; Fairbrother, D. H. *J. Phys. Chem.* **2009**, *113*, 2487−2496.
(49) Plank, H.; Kothleitner, G.; Hofer, F.; Michelitsch, S. G.; Gspan, C.; Hohenau, A.; Krenn, J. *J. Vac. Sci. Technol., B* **2011**, *29*, 051801−051807.
(50) Riazanova, A. V.; Rikers, Y. G. M.; Mulders, J. J. L.; Belova, L. M. *Langmuir* **2012**, *28*, 6185−6191.
(51) Hopf, C.; Schlüter, M.; Schwarz-Selinger, T.; Toussaint, U. v.; Jacob, W. *New J. Phys.* **2008**, *10*, 093022.
(52) Ulbricht, H.; Moos, G.; Hertel, T. *Phys. Rev. B* **2002**, *66*, 075404.
(53) Giannozzi, P.; Car, R.; Scoles, G. *J. Chem. Phys.* **2003**, *118*, 1003−1006.